nature energy

SUPPLEMENTARY INFORMATION

VOLUME: 2 | ARTICLE NUMBER: 17127

In the format provided by the authors and unedited.

Self-optimizing, highly surface-active layered metal dichalcogenide catalysts for hydrogen evolution

Yuanyue Liu[1+], Jingjie Wu[1+], Ken P. Hackenberg[1+],Jing Zhang[1], Y. Morris Wang[2], Yingchao Yang[1], Kunttal Keyshar[1], Jing Gu[3], Tadashi Ogitsu[2], Robert Vajtai[1], Jun Lou[1], Pulickel M. Ajayan[1], Brandon C. Wood*[2], Boris I. Yakobson*[1]

[1]Department of Materials Science and Nano-Engineering, Rice University, Houston, TX 77005.

[2]Lawrence Livermore National Laboratory, Livermore, CA 94550.

[3]Department of Chemistry and Biochemistry, San Diego State University, San Diego, CA, 92182.

[+]These authors contribute equally

*Correspondence to: brandonwood@llnl.gov, biy@rice.edu

Supplementary Discussion: To evaluate the activity of the edges, we calculated the free energies of H adsorption on TaS_2 and NbS_2 edges. Although the structures of TaS_2 and NbS_2 edges at working condition are unknown, and very likely they keep changing during the reaction as the materials are broken into small pieces, we take the most common structure of the MoS_2 edge at HER condition (as shown in the Supplementary figure 18 below)[1,2], as a representative model for TaS_2 and NbS_2 edges.

Our calculations show that the free energies of H adsorption on this specific type of edges are -0.13 eV/H for TaS_2 and -0.26 eV/H for NbS_2. Compared with the free energies of H adsorption on the basal plane, 0.17 eV/H for TaS_2 and 0.01 eV/H for NbS_2, this specific type of edges likely does have some level of activity. However, we point out that these edges are less active than the MoS_2 edge (0.05 eV/H; A closer-to-zero free energy suggests a higher activity, see the main text), which suggests that the better overall performance of NbS_2 and TaS_2 compared to MoS_2 must have significant contributions from other factors. The most likely explanation is basal-plane activity, as our calculations indicate.

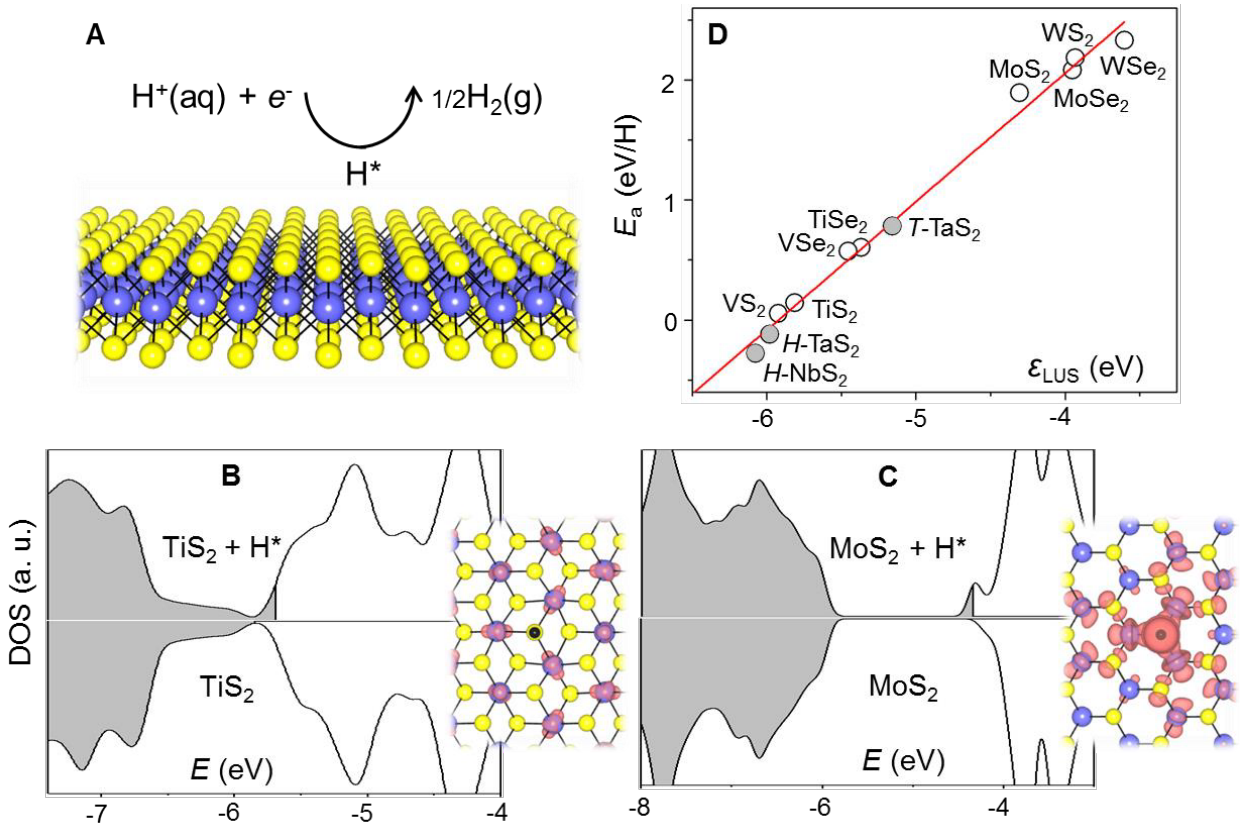

Supplementary figure 1| MX_2 surface activity and its electronic origin. (A) Schematic of MX_2 surface catalyzed HER. M: blue; X: yellow. (**B**) and (**C**) Electronic densities of states (DOS) of representative pristine and H-adsorbed MX_2 systems. DOS plots represent a coverage of H:M = 1:16, with the filled states shown in gray (energies are referenced to vacuum for the pristine case). Left/right panels represent metallic (here, TiS_2) and semiconducting (here, MoS_2) variants. Insets show charge density isosurfaces for states within the energy range of the Fermi level to -0.025 eV below. H: black; charge density isosurface: red. For the metallic system (left panel), H adsorption does not change the overall DOS profile, instead shifting the Fermi level slightly to reflect complete charge transfer from the H adsorbate. The charge density distribution shows that the transferred electrons are delocalized throughout the M layer. For the semiconducting system (right panel), the DOS profile also remains largely intact, and the H occupies a very shallow *n*-type dopant level. The charge density distribution shows that this state is quasi-localized in space. In the dilute adsorption limit, both cases are well described by ε_{LUS}. (**D**) Correlation between the ε_{LUS} descriptor and the surface adsorption energy E_a (Eq. 1, Methods; negative indicates stronger binding) of H for a test series of MX_2 candidates. *H*-NbS_2, *H*-TaS_2 and *T*-TaS_2 are shown as filled circles.

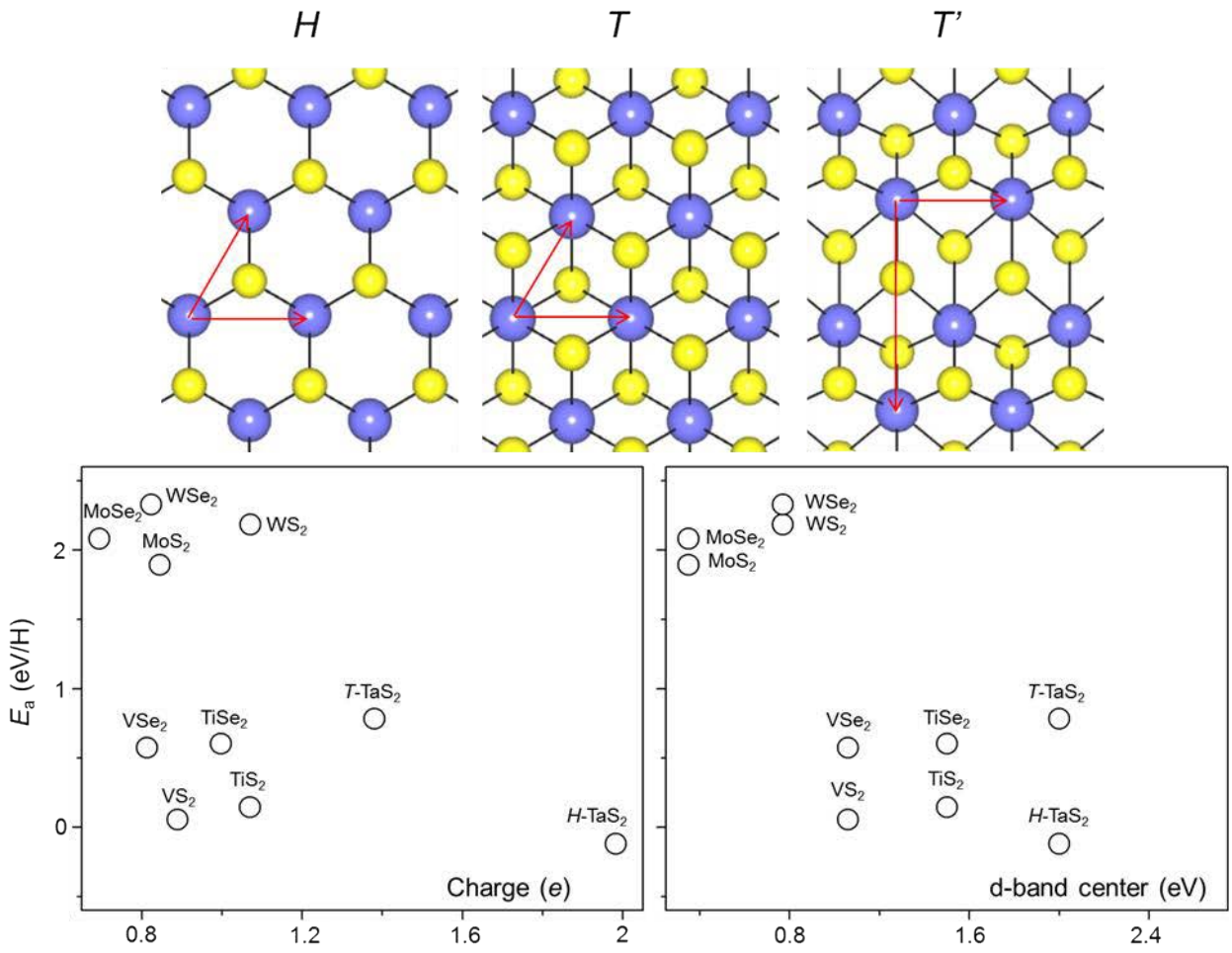

Supplementary figure 2 | Structures of various phases of MX_2 and testing of other common descriptors. Top: the red arrow indicates the primitive cell. Bottom: adsorption energy E_a (Eq. 1, Methods) as a function of the charge on the X atom (left); the *d*-band center of bulk M (right). The *d*-band center values are taken from Ref. [3].

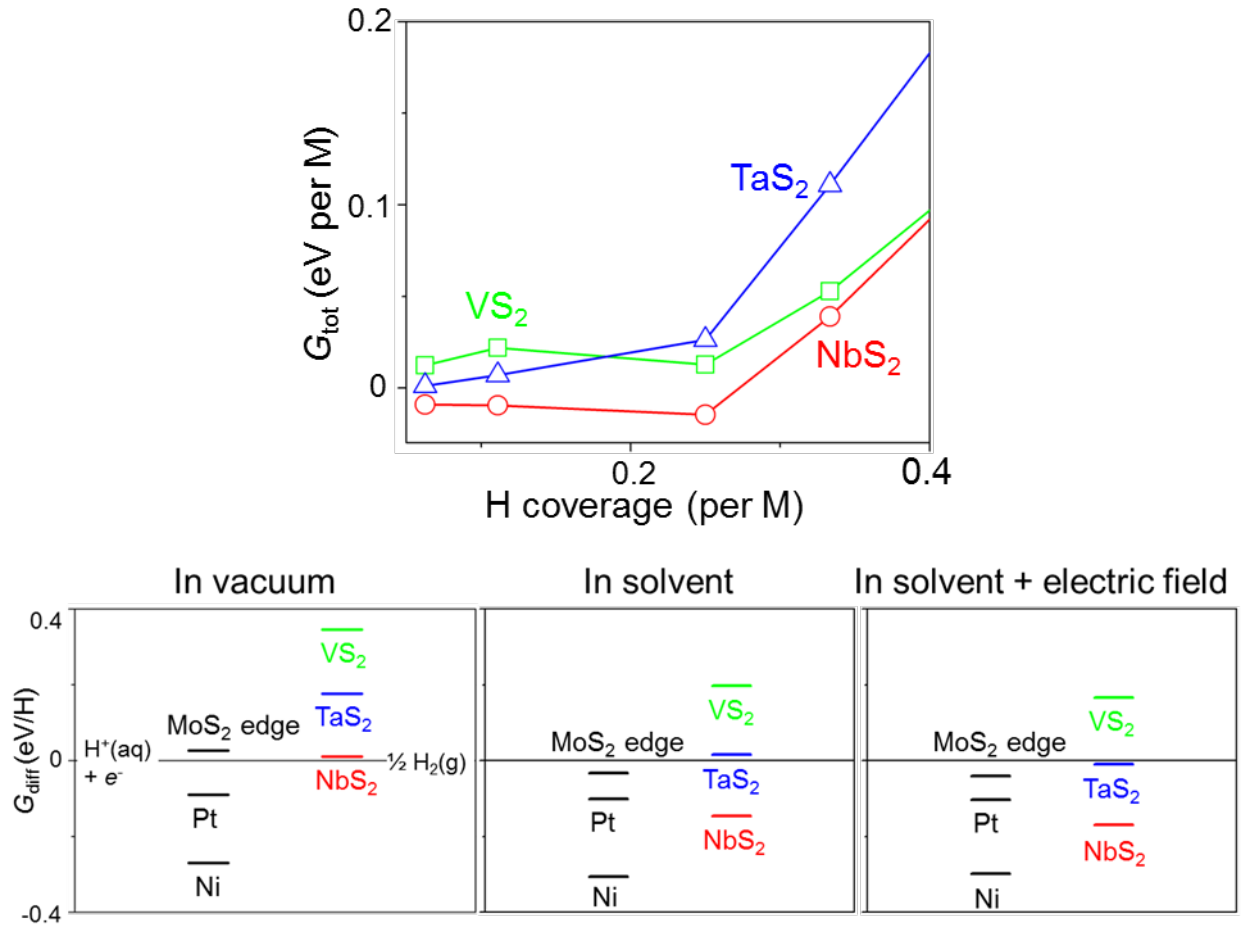

Supplementary figure 3 | Computed G_{diff} and G_{tot} (Eqs. 2 and 3, Methods) for H adsorption on the group-5 MX_2 candidates. Top: Coverage-dependent $G_{tot.}$ Bottom: G_{diff} for the system in vacuum (left), in solvent based on an implicit solvation model (center), and in solvent with a large electric field pointing towards the electrode (right). See Methods for calculation details. For calculation of $G_{diff,}$, results are based on adsorption on a 4x4 supercell; Pt and Ni results assume adsorption on the (111) surface; and the MoS_2 edge is modeled using a nanoribbon with edge structure taken from Ref. [2].

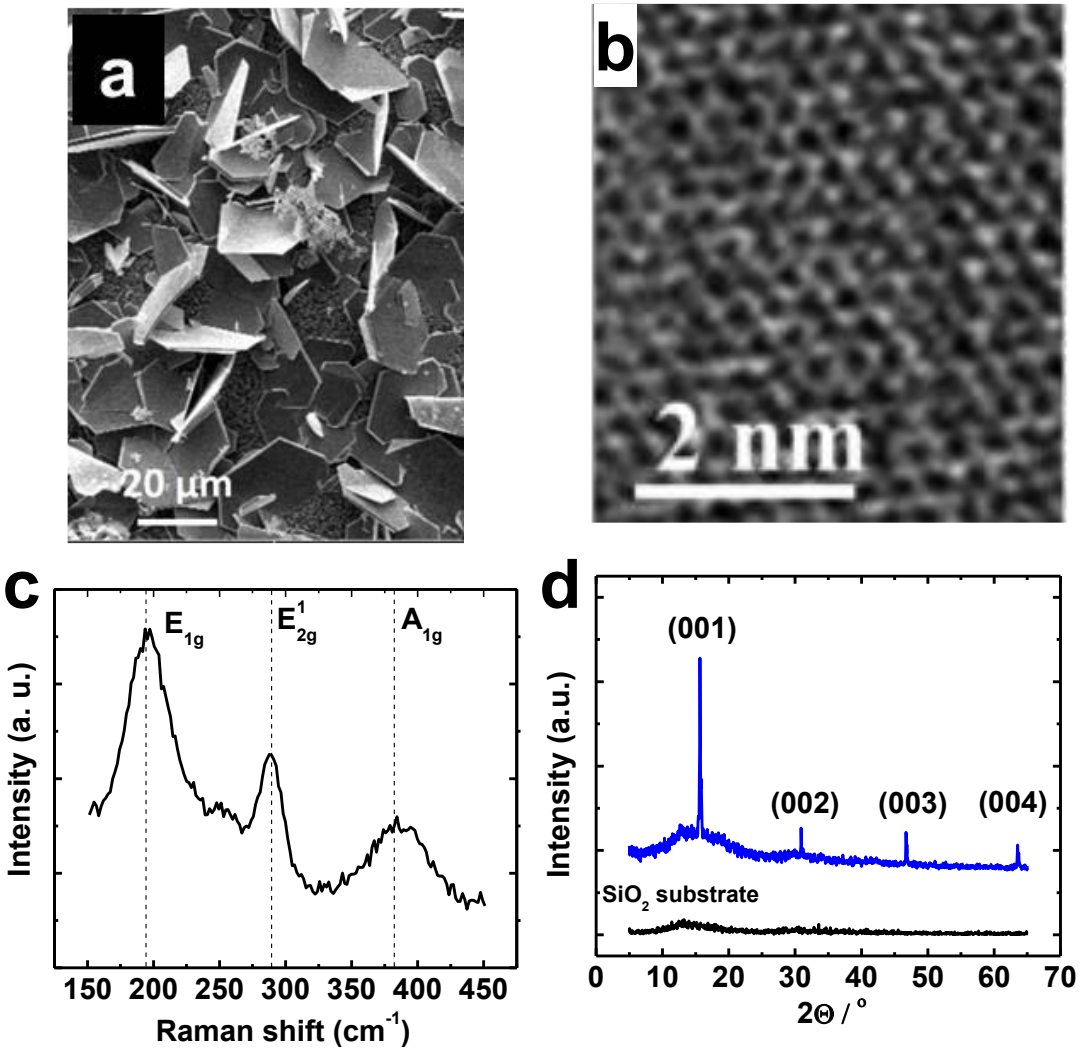

Supplementary figure 4 | Physical characterization of as-grown *H*-TaS_2 flake. (a) SEM image. (b) High-resolution TEM image showing lattice. (c) Raman spectroscopy. (d) XRD pattern of *H*-TaS_2 showing preferred (*00l*) orientation on SiO_2/Si substrate.

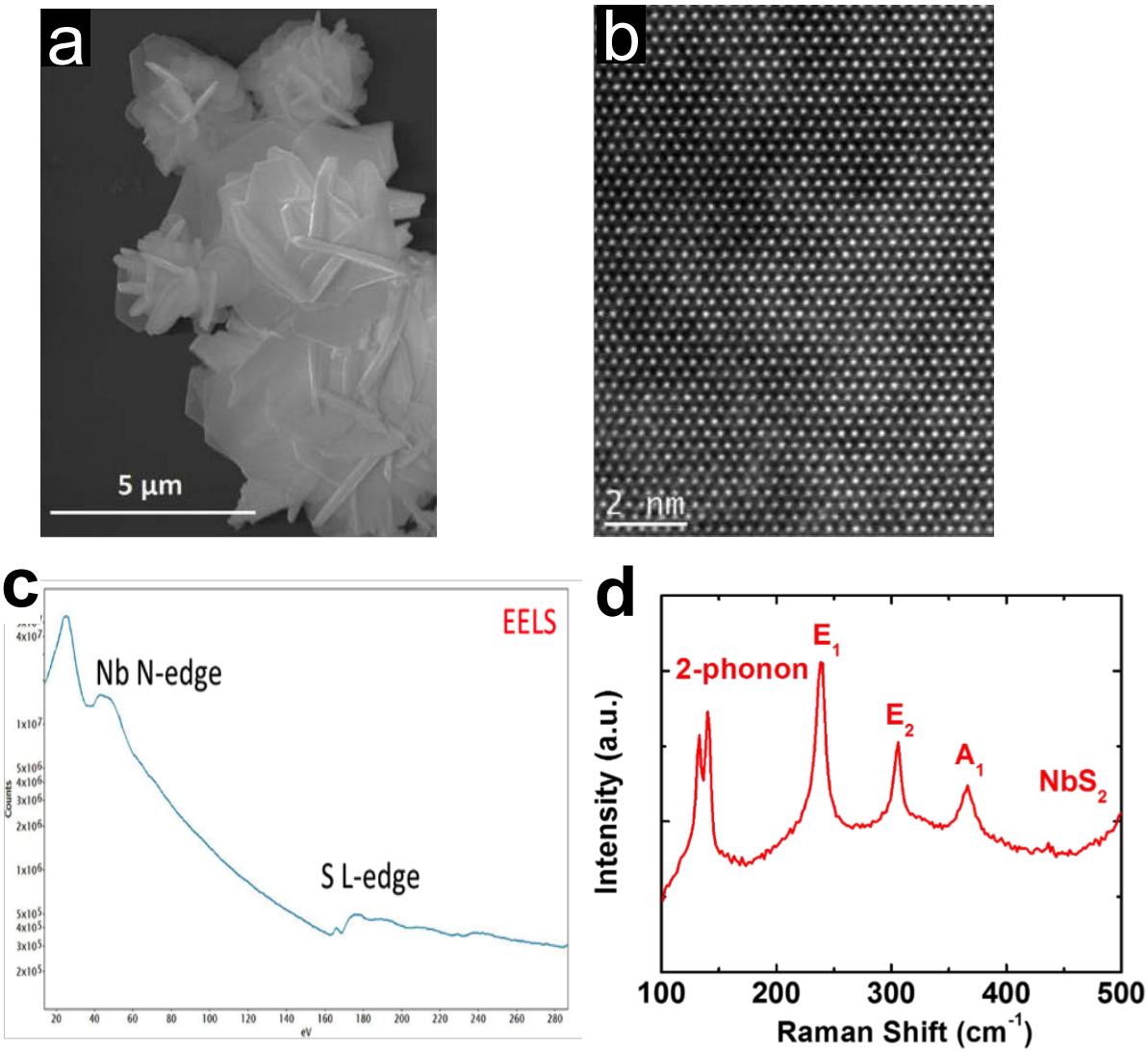

Supplementary figure 5 | Physical characterization of as-grown *H*-NbS_2 flake. (a) SEM image. (b) High-resolution TEM image showing lattice. (h) EELS confirming presence of Nb and S in *H*-NbS_2. (c) Raman spectroscopy.

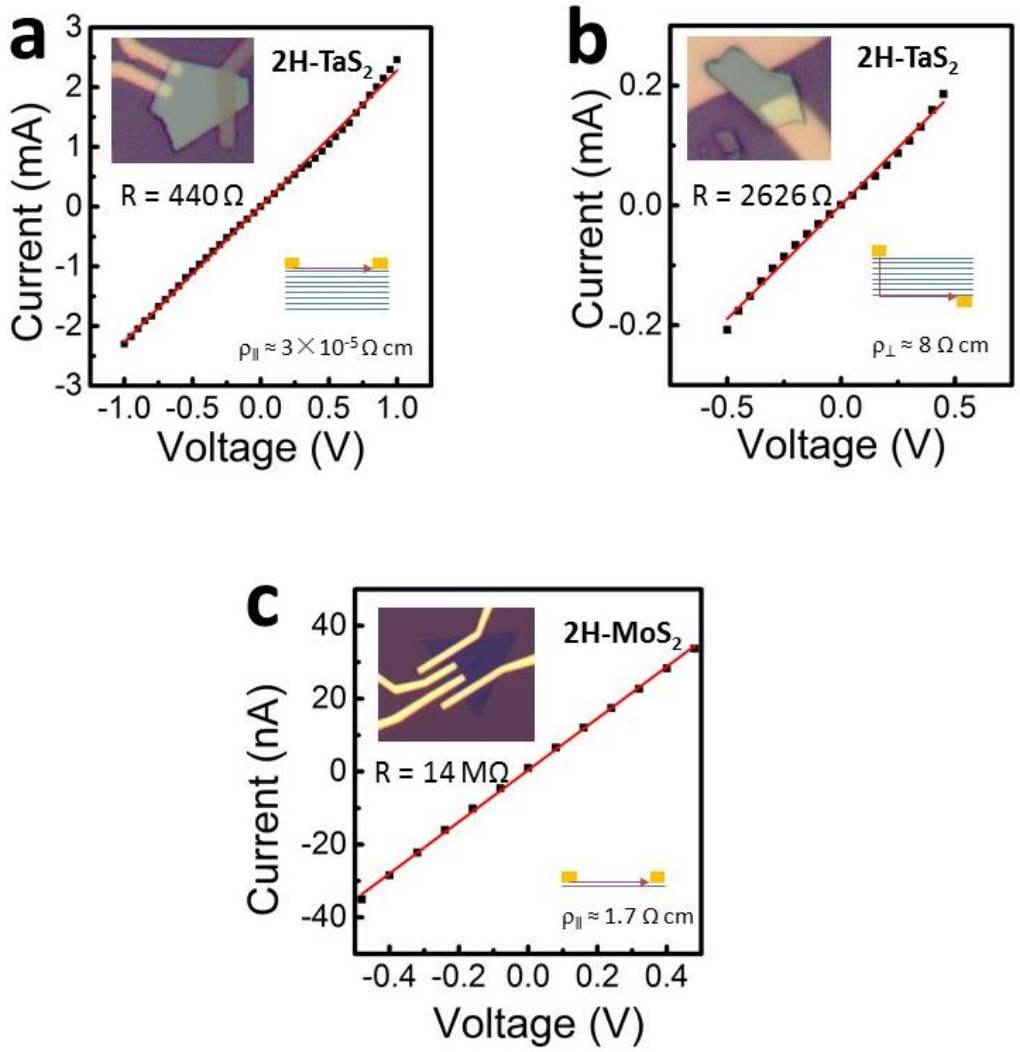

Supplementary figure 6 | Electrical Conductivity of *H*-TaS_2 and *H*-MoS_2 flakes. (a) Measurement of the in-plane and (b) out-of-plane resistivity of pre-cycled *H*-TaS_2, and (c) in-plane resistivity of *H*-MoS_2.

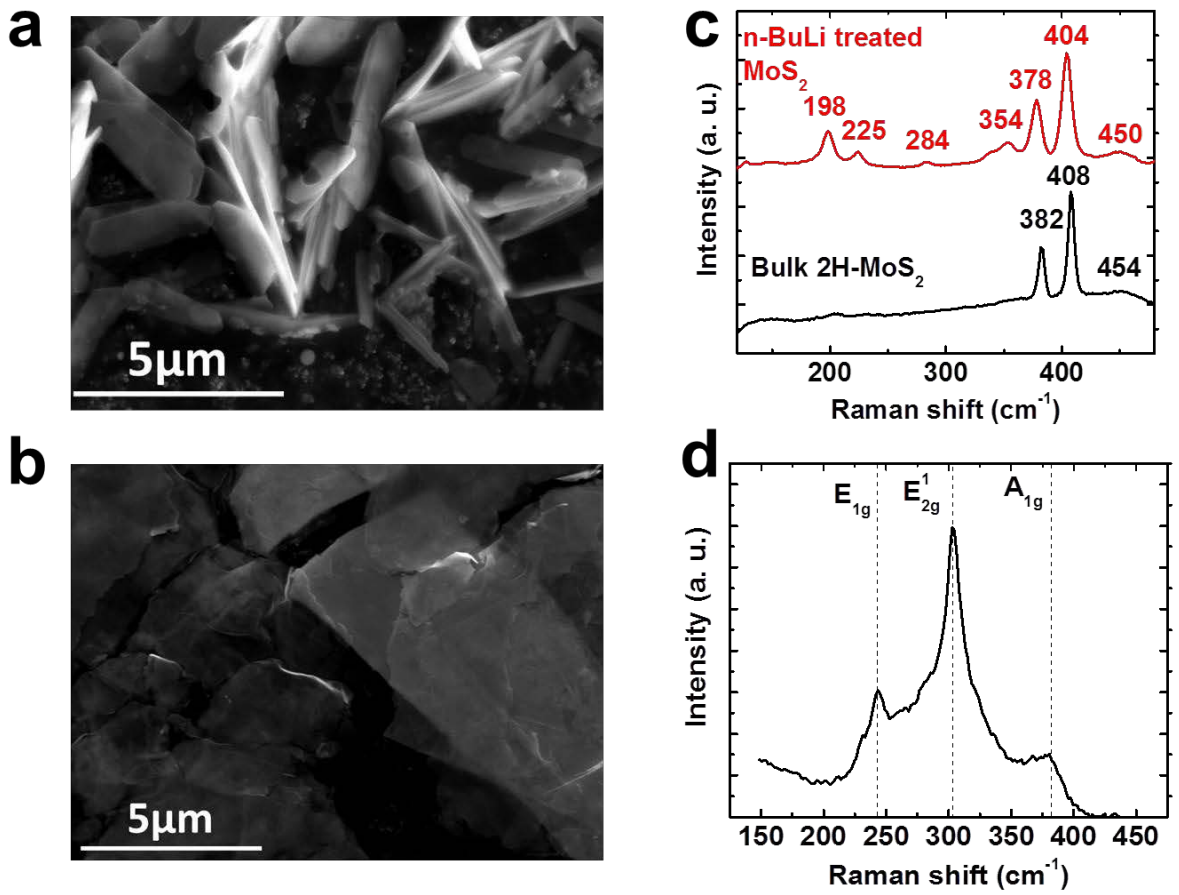

Supplementary figure 7. Physical characterization of *T*-MoS_2 and *T*-TaS_2. SEM images for (a) *T*-MoS_2 and (b) *T*-TaS_2. Raman spectroscopy for (c) *T*-MoS_2 and (d) *T*-TaS_2 . The *T*-MoS_2 has a typical thickness around 100 nm which is comparable to the TaS_2 after 5000 cycles. The emergence of new Raman shifts at 198, 225, and 284 cm^{-1} associated with the phonon modes of *T*-MoS_2, clearly confirm the formation of *T*-MoS_2 from exfoliation treatment of commercial *H*-MoS_2 plates.

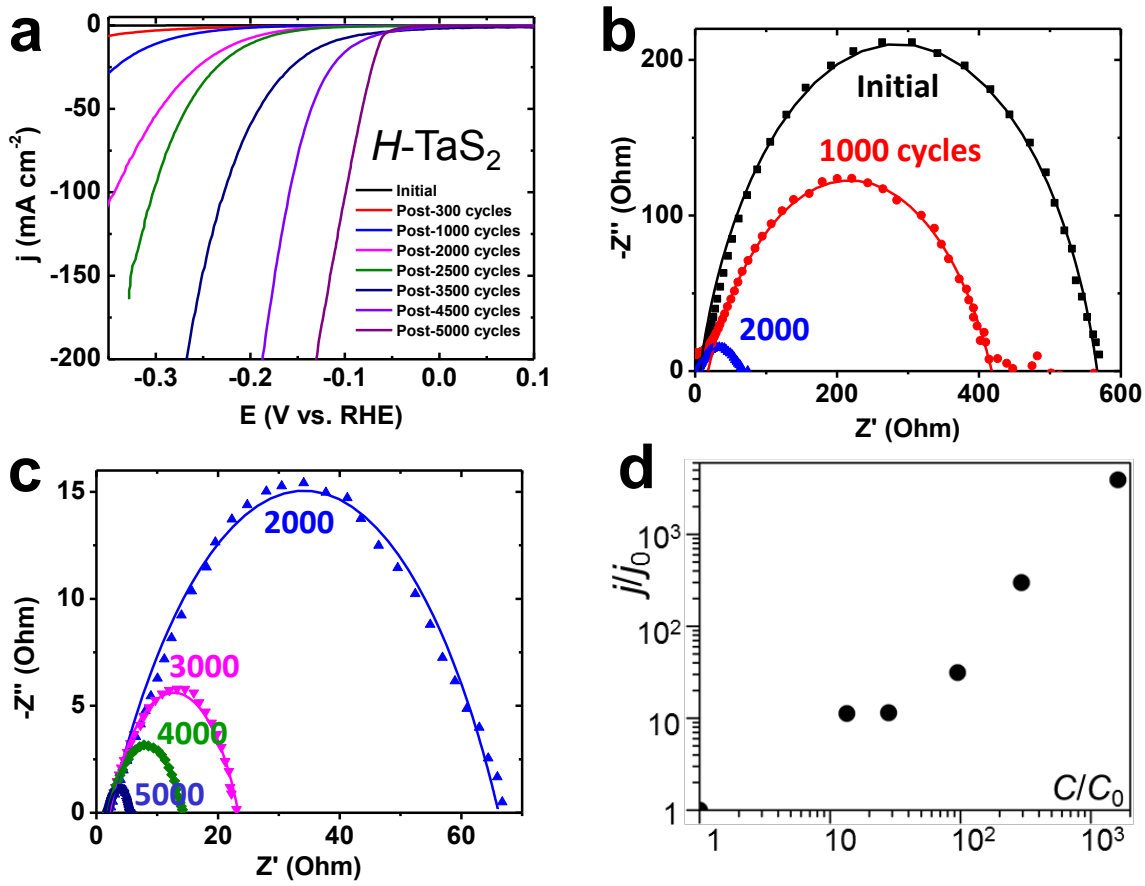

Supplementary figure 8 | Electrochemical evolution recorded periodically during potential cycling for *H*-TaS_2 electrode. (a) Polarization curves recorded after different cycles. The initial polarization curve was recorded after 4 cycles. (b-c) EIS after correspondent cycles. Solid lines are fit to the equivalent circuit model described in Methods. (d) Relative change of current density *j* (at -0.1 V vs. RHE) for *H*-TaS_2 as a function of the change in the effective double-layer capacitance *C* for *H*-TaS_2. The capacitance is derived from the constant phase element (CPE) in the EIS equivalent circuit. The power of *n* used in the CPE fits are 0.78, 0.72, 0.76, 0.68, 0.70, 0.72 for 2, 1000, 2000, 3000, 4000 and 5000 cycles, respectively.

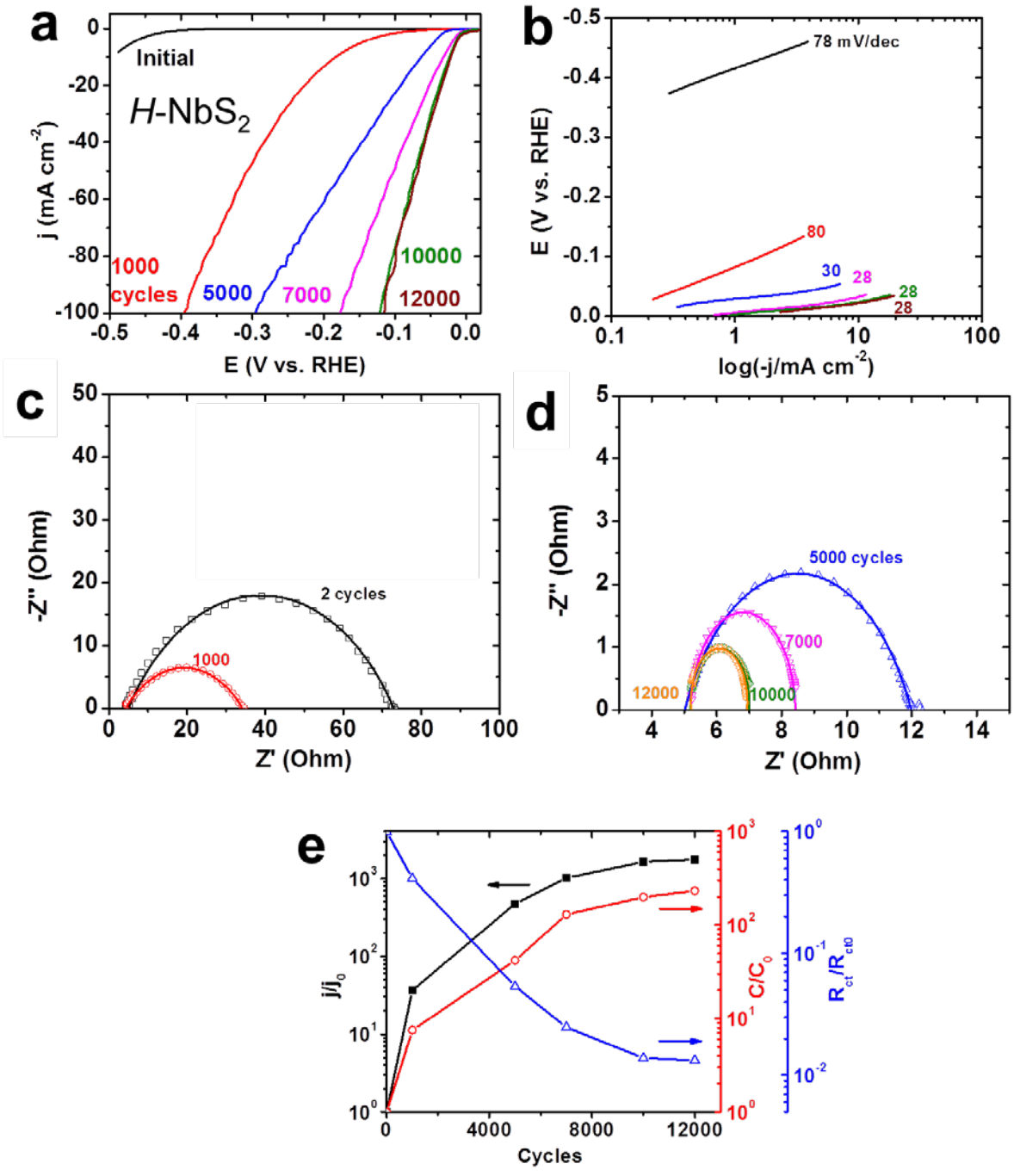

Supplementary figure 9 | Electrochemical evolution recorded periodically during potential cycling for *H*-NbS_2 electrode. (a) Polarization curves recorded after different cycles. The initial polarization curve was recorded after 2 cycles. (b) The corresponding Tafel slope evolution. (c-d) EIS after correspondent cycles. Solid lines are fits to the equivalent circuit model described in Methods. (e) Cycle-dependent evolution of current (recorded at -0.1 V vs. RHE), charge transfer resistivity, and capacitance for *H*-NbS_2.

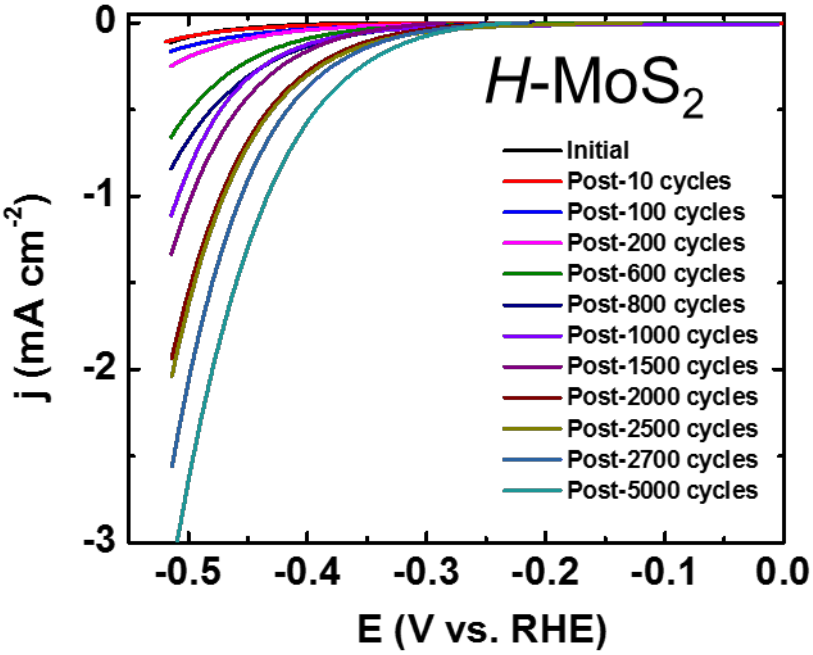

Supplementary figure 10 | Polarization curves recorded periodically during potential cycling for *H*-MoS_2 electrode. The initial polarization curve was recorded after 2 cycles.

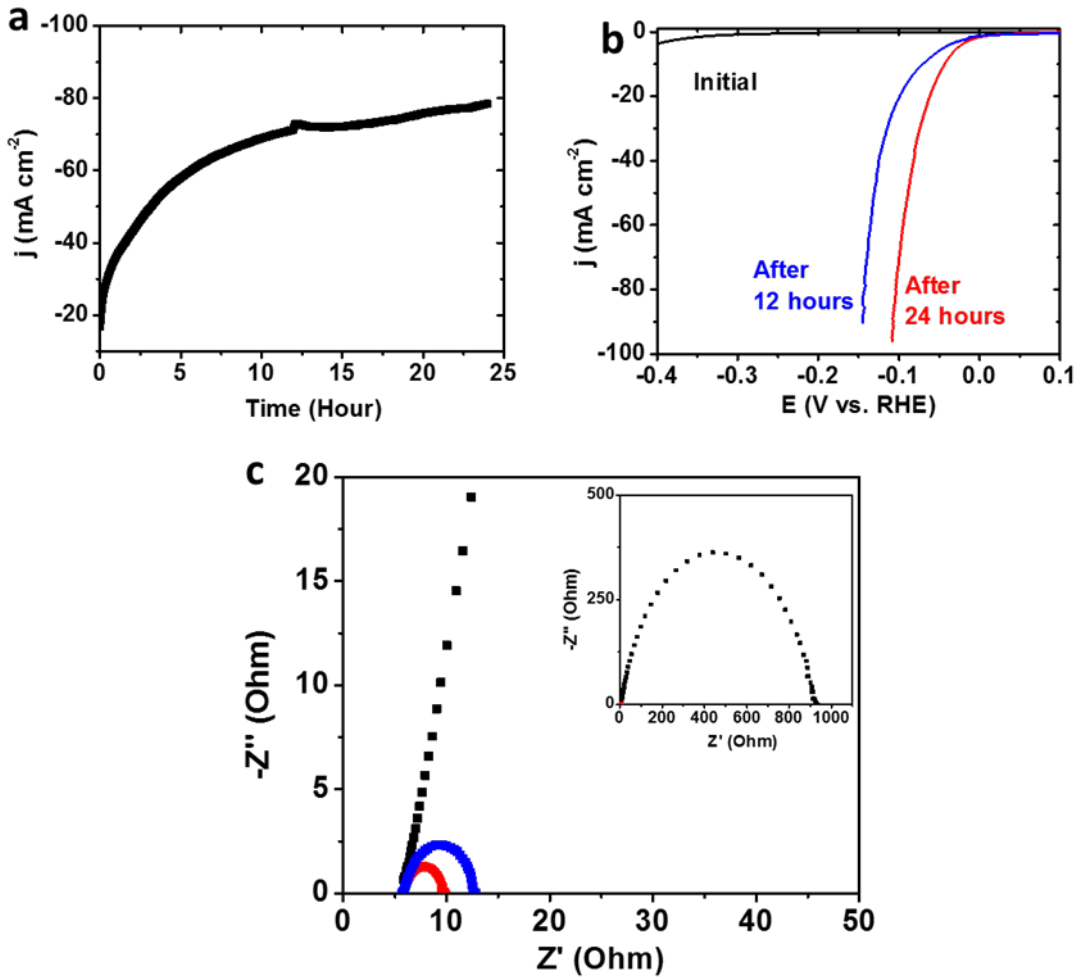

Supplementary figure 11 | HER of *H*-TaS_2 under potentiostatic operation. (a) Chronoamperometric response at constant potential of -0.54 V vs. RHE (not iR corrected). (b) Linear sweep voltammetry of initial and after 12 and 24 hours. (c) Corresponding EIS data.

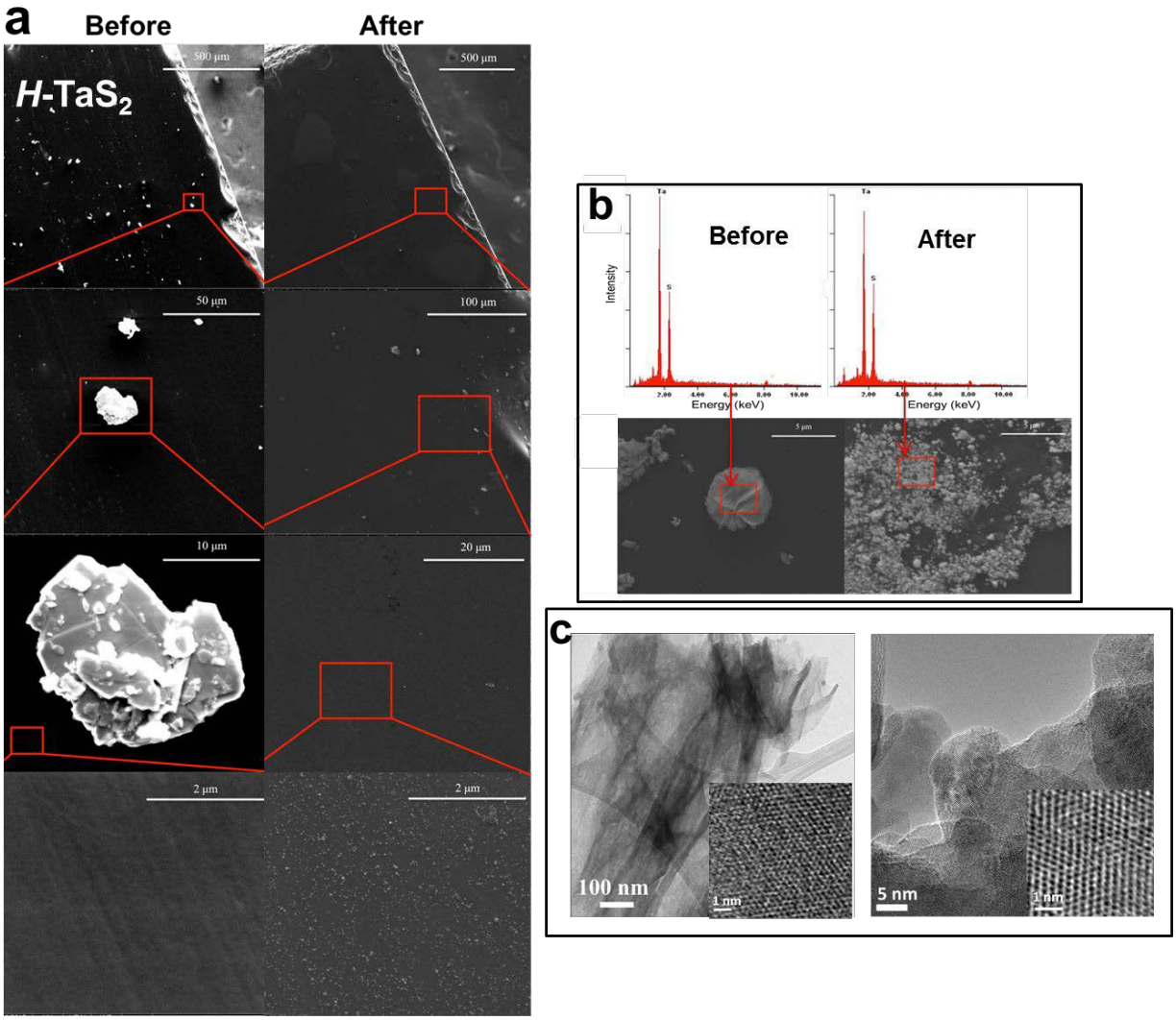

Supplementary figure 12 | Morphological, chemical and structural characterization of *H*-TaS_2 on a glassy carbon plate before and after cycling. (a) SEM images showing morphological evolution of *H*-TaS_2 at different magnifications before (left) and after (right) 5000 cycles. The bottom left shows a blank image, confirming no nano-scaled *H*-TaS_2 before cycling. (b) EDS characterization of *H*-TaS_2 before (left) and after (right) cycling for densely covered regions shown in the SEM images below. (c) TEM images for *H*-TaS_2 before (left) and after (right). Insets are HETEM showing no crystalline structure change.

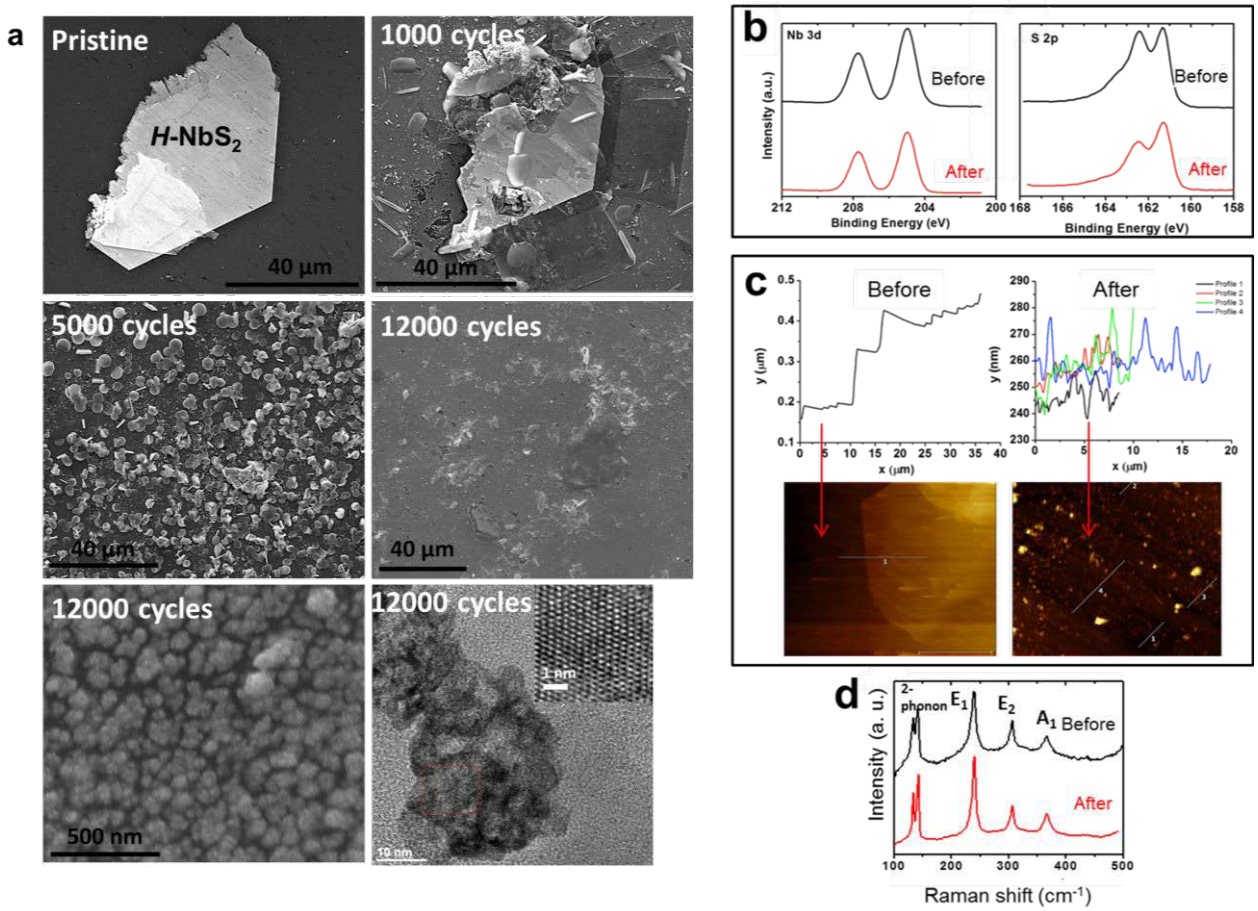

Supplementary figure 13 | Morphological, chemical and structural characterization of *H*-NbS_2 on a glassy carbon plate before and after cycling. (a) SEM and TEM images showing morphological evolution of *H*-NbS_2 at different cycles. The inset at the bottom right image shows the HRTEM of *H*-NbS_2 after 12000 cycles (b) XPS data for fine scan of S 2p and Nb 3d of *H*-NbS_2 cycling. (c) Thickness profiles for *H*-NbS_2 before (left) and after (right) cycling, based on the AFM images below. Four thickness profiles are shown for the cycled sample to confirm thickness uniformity. (d) Raman spectroscopy of *H*-NbS_2 before and after cycling.

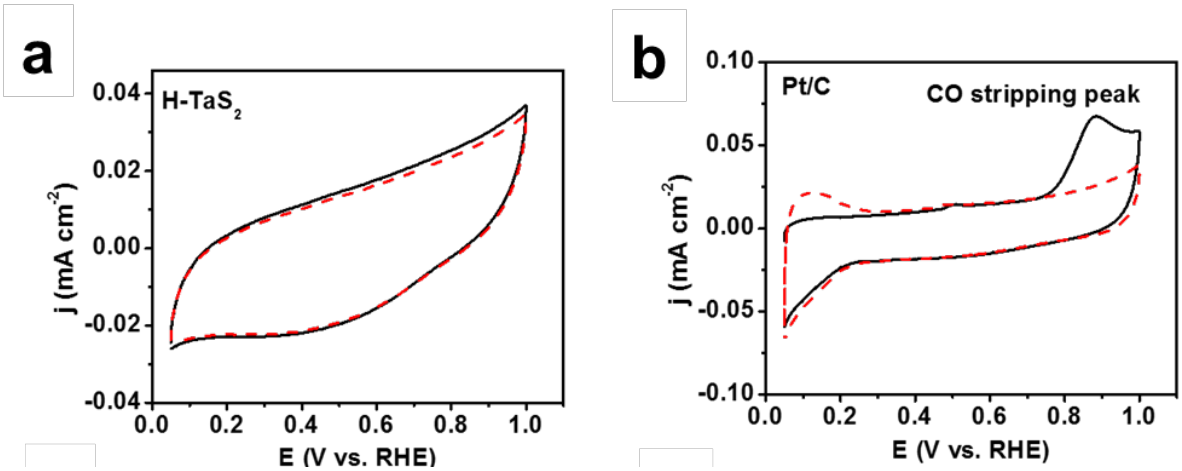

Supplementary figure 14 | Absence of contaminants in *H*-TaS_2 as evidenced by CO stripping voltammetry results. (a) CO stripping voltammetry for a long-term cycled *H*-TaS_2 and (b) a reference Pt/C (Pt loading 0.3 μg cm^{-2}) electrode in CO-free solution of 0.5 M H_2SO_4. Solid line is CO stripping, dashed line is background cyclic voltammogram collected immediately after CO stripping. The CO is adsorbed at a constant potential of 0.20 V vs. RHE for 5 min. Scan rate is 50 mV/s.

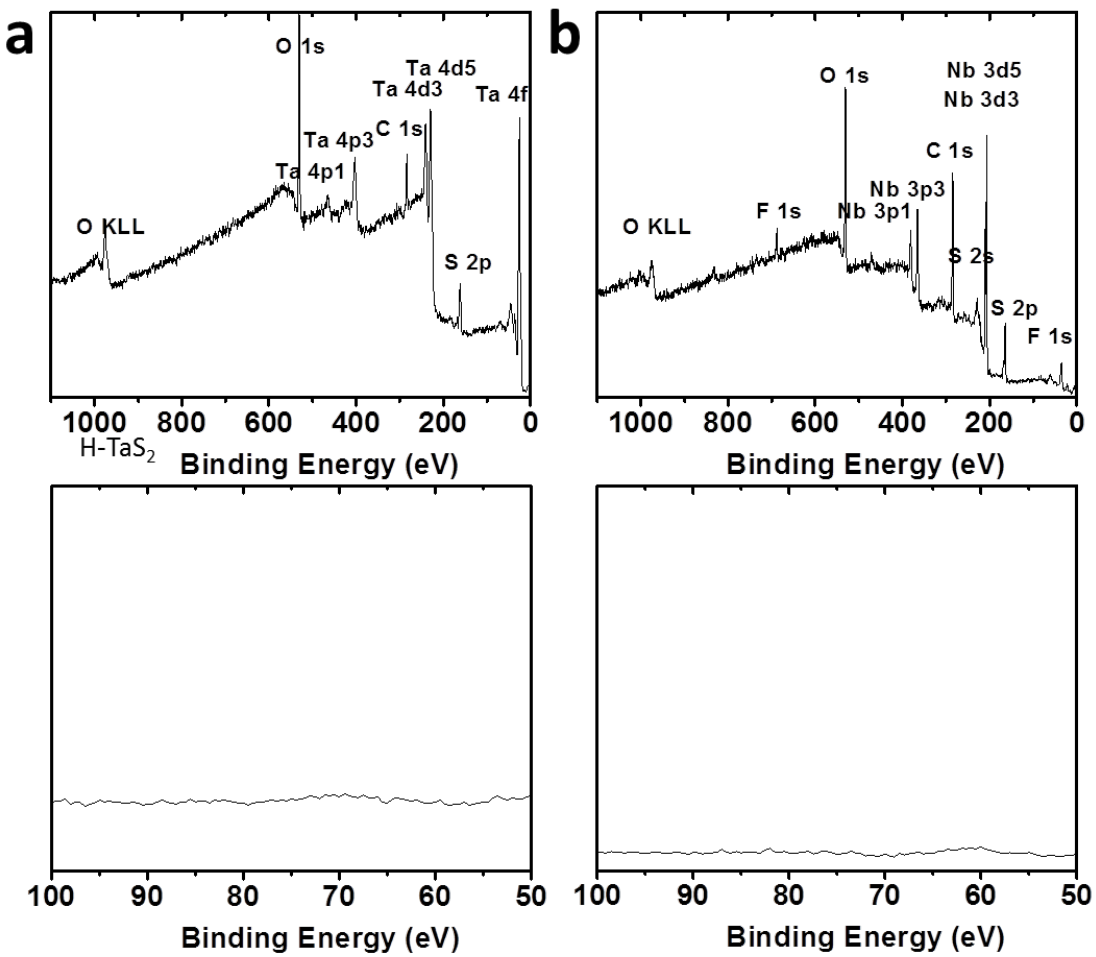

Supplementary figure 15 | Absence of contaminants in *H*-TaS_2 and *H*-NbS_2as evidenced by XPS survey scan of electrodes after cycling. (a) H-TaS_2 and (b) H-NbS_2. Bottom panels show zoomed-in regions of 50-100 eV. The survey scan shows no other metal contaminations on the electrodes or below the detecting limit.

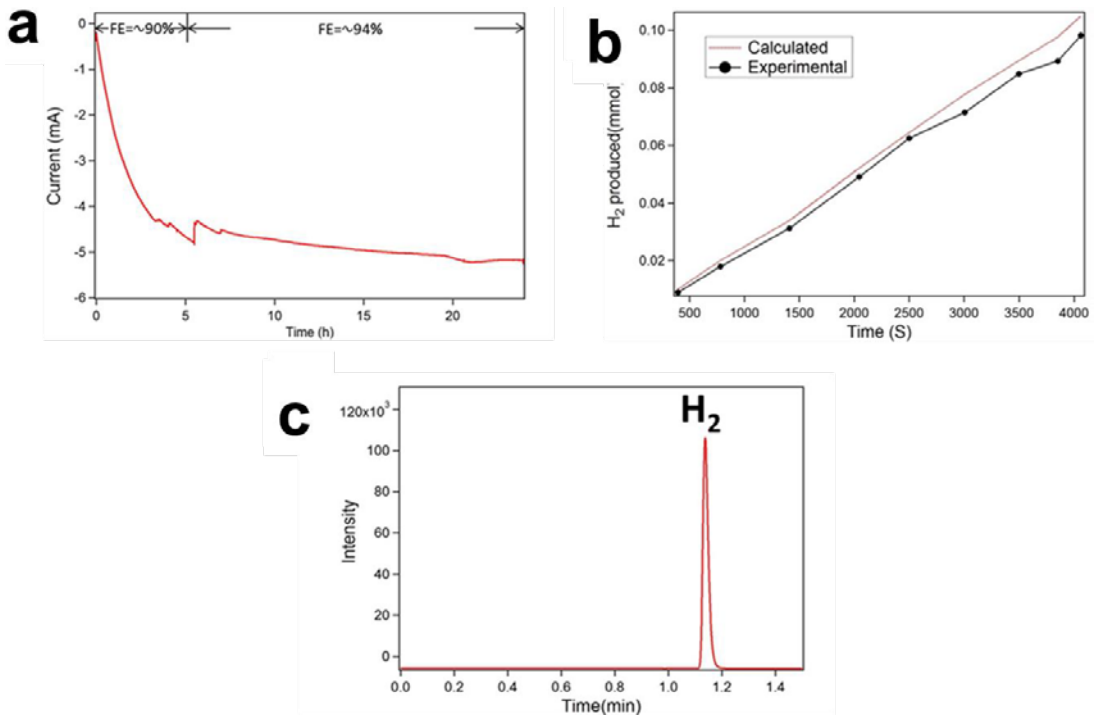

Supplementary figure 16 | Faradaic efficiency of H_2 evolution reaction on *H*-TaS_2 electrode. (a) Current versus time at -0.4 V vs. RHE, with (b) periodically measured production moles of H_2. The red line represents theoretical production moles calculated from the charges passed during electrolysis. (c) Gas chromatography trace of H_2 collected from the HER compartment.

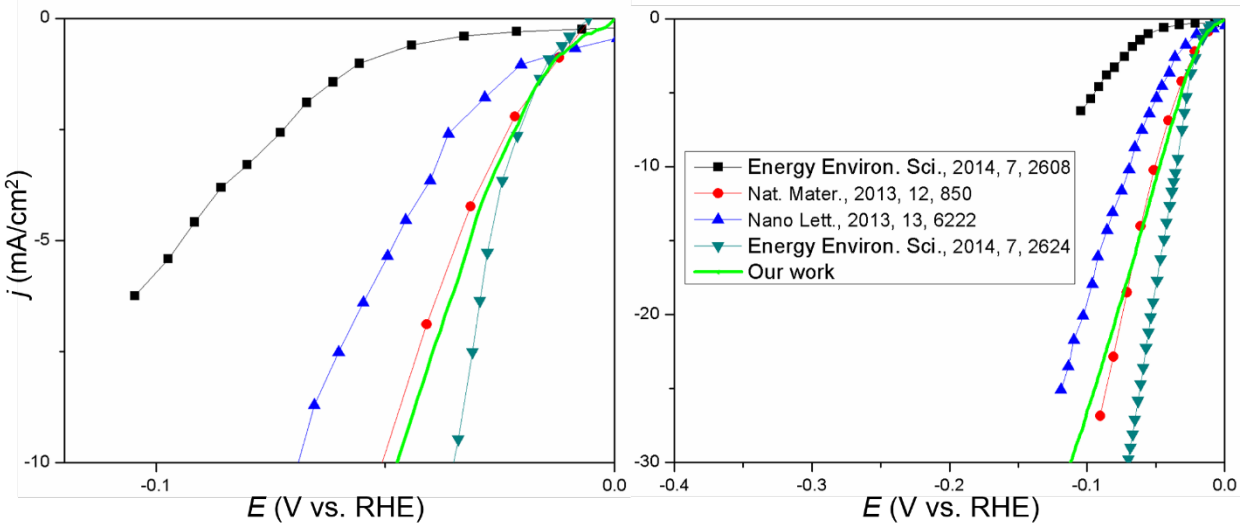

Supplementary figure 17 | Polarization curves of Pt shown in different scales. The literature results are included for comparison.

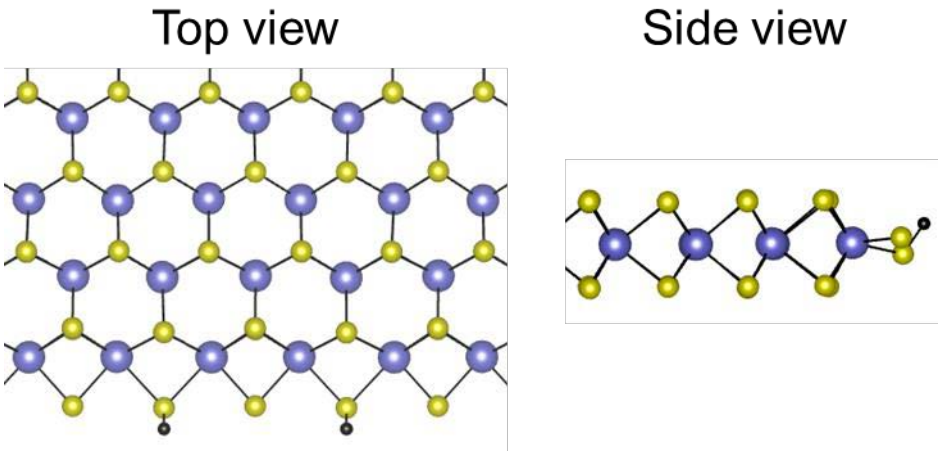

Supplementary figure 18| The most common structure of MoS_2 edge at HER condition (see JACS 2015 137 6692; JACS 2005 127 5308 etc).

Supplementary table 1. Comparison of HER activity

Sample	Catalyst loading ($\mu g/cm^2$)	j_0 (A/cm^2)	Tafel slope (mV/decade)	|j| @ -0.15 V vs. RHE (mA/cm^2)	|V| vs. RHE @ j=-10 mA/cm^2 (V)	Ref
Nano particulate MoS_2	N/A	$1.3\text{-}3.7\times10^{-7}$	55-60	0.1	0.17	4
Particulate MoS_2	4	4.6×10^{-6}	120	0.5	0.3	5
Double gyroid MoS_2	60	6.9×10^{-7}	50	1	0.28	6
Edge exposed MoS_2 film	8.5	2.2×10^{-6}	105-120	0.06	>0.4	7
Edge exposed MoS_2 film	22	$1.71\text{-}3.40\times 10^{-6}$	115-123	0.1	0.21	8
30 nm MoS_2	3400-3900	5.0×10^{-5}	66	10.3	0.15	9
***T*- MoS_2**	50	N/A	40	1	0.2	10
***T*- MoS_2**	N/A	N/A	43	2	0.2	11
MoS_2/RGO	285	5.1×10^{-6}	41	8	0.16	12
Defect-Rich MoS_2	285	8.9×10^{-6}	50	3	0.2	13
Electrodeposited MoS_2	N/A	N/A	106	2	>0.4	14
MoS_2/CNT-	650	2.91×10^{-5}	100	2	0.28	15

graphene						
NanoflakesWS_2	350	N/A	48	1	>0.4	[16]
WS_2/RGO	400	N/A	58	2	0.26	[17]
***T*-WS_2**	6.5	1×10^{-6}	60	1	0.23	[18]
***T*-WS_2**	1000±200	$<10^{-4}$	70	14	0.14	[19]
MoS_X/CNT	102	33.11×10^{-6}	40	25	0.11	[20]
***H*-MoS_2**	100	3.4×10^{-6}	120	0.08	>0.4	This work
***T*-MoS_2**	50	2.5×10^{-6}	78	0.2	0.29	This work
***T*-TaS_2**	80	6.4×10^{-8}	92	0.02	>0.4	This work
***H*-TaS_2**	55	7.8×10^{-5}	37	160	0.06	This work
***H*-NbS_2**	10	1.3×10^{-3}	28	128	0.05	This work

Supplementary references:

1 Huang, Y., Nielsen, R. J., Goddard, W. A. & Soriaga, M. P. The Reaction Mechanism with Free Energy Barriers for Electrochemical Dihydrogen Evolution on MoS2. *J. Am. Chem. Soc.* **137**, 6692-6698 (2015).

2 Hinnemann, B. *et al.* Biomimetic Hydrogen Evolution: MoS2 Nanoparticles as Catalyst for Hydrogen Evolution. *J. Am. Chem. Soc.* **127**, 5308-5309 (2005).

3 Hammer, B. & Nørskov, J. K. in *Advances in Catalysis* Vol. Volume 45 (ed Helmut Knozinger Bruce C. Gates) 71-129 (Academic Press, 2000).

4 Jaramillo, T. F. *et al.* Identification of Active Edge Sites for Electrochemical H2 Evolution from MoS2 Nanocatalysts. *Science* **317**, 100-102 (2007).

5 Bonde, J., Moses, P. G., Jaramillo, T. F., Norskov, J. K. & Chorkendorff, I. Hydrogen evolution on nano-particulate transition metal sulfides. *Faraday Discussions* **140**, 219-231 (2009).

6 Kibsgaard, J., Chen, Z., Reinecke, B. N. & Jaramillo, T. F. Engineering the surface structure of MoS2 to preferentially expose active edge sites for electrocatalysis. *Nature Mate.* **11**, 963-969 (2012).

7 Kong, D. *et al.* Synthesis of MoS2 and MoSe2 Films with Vertically Aligned Layers. *Nano Lett.* **13**, 1341-1347 (2013).

8 Wang, H. T. *et al.* Electrochemical tuning of vertically aligned MoS2 nanofilms and its application in improving hydrogen evolution reaction. *Proceedings of the National Academy of Sciences of the United States of America* **110**, 19701-19706 (2013).

9 Wang, H. *et al.* Electrochemical Tuning of MoS2 Nanoparticles on Three-Dimensional Substrate for Efficient Hydrogen Evolution. *ACS Nano* **8**, 4940-4947 (2014).

10 Voiry, D. *et al.* Conducting MoS2 Nanosheets as Catalysts for Hydrogen Evolution Reaction. *Nano Lett.* **13**, 6222-6227 (2013).

11 Lukowski, M. A. *et al.* Enhanced Hydrogen Evolution Catalysis from Chemically Exfoliated Metallic MoS2 Nanosheets. *J. Am. Chem. Soc.* **135**, 10274-10277 (2013).

12 Li, Y. *et al.* MoS2 Nanoparticles Grown on Graphene: An Advanced Catalyst for the Hydrogen Evolution Reaction. *J. Am. Chem. Soc.* **133**, 7296-7299 (2011).
13 Xie, J. *et al.* Defect-Rich MoS2 Ultrathin Nanosheets with Additional Active Edge Sites for Enhanced Electrocatalytic Hydrogen Evolution. *Advanced Materials* **25**, 5807-5813 (2013).
14 Murugesan, S. *et al.* Room Temperature Electrodeposition of Molybdenum Sulfide for Catalytic and Photoluminescence Applications. *ACS Nano* **7**, 8199-8205 (2013).
15 Youn, D. H. *et al.* Highly Active and Stable Hydrogen Evolution Electrocatalysts Based on Molybdenum Compounds on Carbon Nanotube–Graphene Hybrid Support. *ACS Nano* **8**, 5164-5173 (2014).
16 Cheng, L. *et al.* Ultrathin WS2 Nanoflakes as a High-Performance Electrocatalyst for the Hydrogen Evolution Reaction. *Angewandte Chemie International Edition*, n/a-n/a (2014).
17 Yang, J. *et al.* Two-Dimensional Hybrid Nanosheets of Tungsten Disulfide and Reduced Graphene Oxide as Catalysts for Enhanced Hydrogen Evolution. *Angewandte Chemie International Edition* **52**, 13751-13754 (2013).
18 Voiry, D. *et al.* Enhanced catalytic activity in strained chemically exfoliated WS2 nanosheets for hydrogen evolution. *Nature Mate.* **12**, 850-855 (2013).
19 Lukowski, M. A. *et al.* Highly active hydrogen evolution catalysis from metallic WS2 nanosheets. *Energy Environ. Sci.* **7**, 2608-2613 (2014).
20 Li, D. J. *et al.* Molybdenum Sulfide/N-Doped CNT Forest Hybrid Catalysts for High-Performance Hydrogen Evolution Reaction. *Nano Lett.* **14**, 1228-1233 (2014).